Dynamics of spatially modulated kinks in shallow granular layers

2014 New J. Phys. 16 043032

(http://iopscience.iop.org/1367-2630/16/4/043032)

New Journal of Physics
The open access journal at the forefront of physics
Deutsche Physikalische Gesellschaft DPG | IOP Institute of Physics

Dynamics of spatially modulated kinks in shallow granular layers

J E Macías and C Falcón
Departamento de Física, Facultad de Ciencias Físicas y Matemáticas, Universidad de Chile, Casilla 487-3, Santiago, Chile
E-mail: cfalcon@ing.uchile.cl

Received 18 November 2013, revised 12 February 2014
Accepted for publication 11 March 2014
Published 30 April 2014
New Journal of Physics **16** (2014) 043032
doi:10.1088/1367-2630/16/4/043032

Abstract
We report on the experimental observation and characterization of the bifurcation diagram, dynamical properties and fluctuations of spatially modulated kinks in a shallow one-dimensional fluidized granular layer subjected to a periodic air flow. We show the appearance of these solutions as the layer undergoes a parametric instability. Due to the inherent fluctuations of the granular layer, the kink profile exhibits an effective wavelength, termed the *precursor*, which modulates spatially the homogeneous states and drastically modifies the kink dynamics. We characterize the average and fluctuating properties of this solution. The long-term evolution of these kinks is dominated by a hopping dynamics, related directly to the underlying spatial structure and inherent fluctuation. The properties of this motion can be described by a Brownian particle in a symmetric periodic potential. Both the noise intensity of the Brownian fluctuations and the amplitude and periodicity of the potential arise from the underlying precursor structure.

Keywords: granular matter, mean first passage time, fronts, pattern forming systems

1. Introduction

In recent years, granular matter has become an inspiring source of new ideas, concepts and phenomena [1, 2]. It can display both coherent structures and fluctuations [3], and the coexistence of different states or phases [4–6] depending on the interplay between the injection and dissipation of energy, particles or momenta. The different domains of phases or states are separated by interfaces which have fluctuating and complex dynamics, and whose properties describe the state of the granular system over long times. These interfaces or spatial connections are known as fronts [5]. The description of these interfaces follows a particle-type evolution, as they can be characterized by a discrete set of continuous parameters such as the position, width or speed [7], to name a few. When these fronts spatially connect two symmetric states they are called *kinks*. From the early stages of classical and quantum field theory, kinks have played a key role in understanding the dynamics of several physical phenomena [8].

A way to generate symmetric states that coexist is through the parametrical amplification of nonlinear systems through instabilities [6], where the symmetric states are out of phase in half the period of the system [9]. Kinks have been observed naturally in two-dimensional vertically oscillated fluid layers [10] and also in two-dimensional vertically vibrofluidized granular layers [11]. Although several studies have been performed in two-dimensional fluidized granular layers, only a handful of studies on one-dimensional fluidized granular layers where kinks connect homogeneous states have been reported experimentally [12, 13] and numerically [14, 15]. To our knowledge, there is no observation of kink solutions connecting spatially modulated states [16].

A first attempt to study the formation of spatially modulated kinks was performed in [17], where such structures were first observed in a quasi-one-dimensional granular layer fluidized via a periodic air flow. In [17], the appearance of these kinks through a parametric instability of the granular layer is shown experimentally, and some of the properties of these structures, such as the width and height of the granular kink, were characterized. Nevertheless, an appropriated description of the dynamical features of spatially modulated kinks was lacking. As a special case, we can mention the necessity of a model capable of predicting, for instance, the long-time dynamics displayed by spatially modulated kinks, taking into account the spatiotemporal features of these structures.

In this paper, we focus on the experimental observation and characterization of the bifurcation diagram, dynamical properties and fluctuations of kinks appearing in a shallow one-dimensional fluidized granular layer subjected to a periodic air flow, similar to the ones observed in [17]. We show that the appearance of these solutions (as well as stationary patterns for stronger periodic air flow) is mediated by a parametric instability of the fluidized granular layer. A granular kink separates regions in which areal densities are the same but that are out of phase. This effect comes from the nature of the parametric instability of the oscillating granular layer. The structure of the fluctuating kink profile exhibits an effective wavelength that modulates spatially the homogeneous states and drastically modifies the kink dynamics. The long-term evolution of these kinks is dominated by a hopping dynamics, related directly to the underlying spatial structure, which can be described using a simple model of a Brownian particle (describing the position of the core of the kink) in a symmetric periodic potential. This interpretation presents a way to understand the generation of an effective potential from the underlying fluctuating structure around the core of the kink.

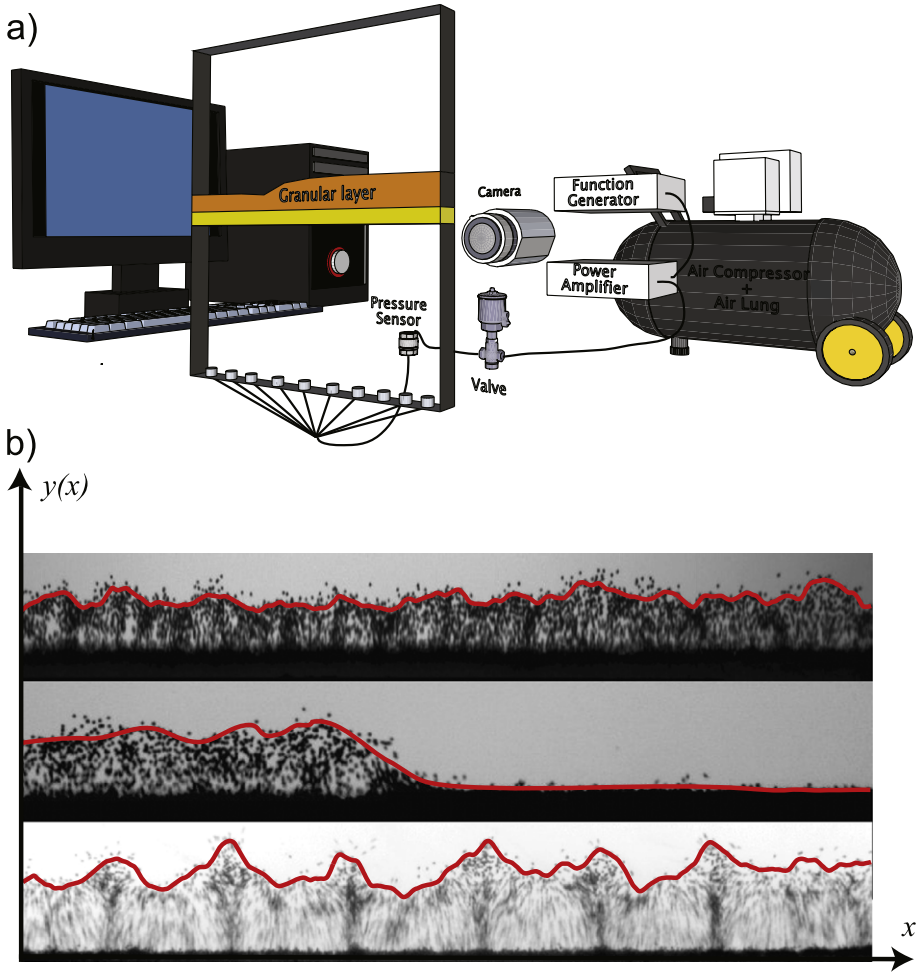

Figure 1. (a) Scheme of the experimental setup. The experimental cell (center frame) holding a shallow granular layer is excited via a periodic air flow. (b) Images of the homogeneous layer, a granular kink and a stationary pattern, and their respective surface interface computed (continuous line).

This manuscript is organized as follows. In section 2, we present the experimental setup and measuring techniques used in this work. In section 3, the experimental results are shown, describing mainly the bifurcation and phase diagram of the parametrically excited granular layer, the structure of the kink solution, its dynamical properties and long-term evolution. Finally, in section 4, we present a simple model to describe the observed long-term dynamics of the kink and contrast it with the acquired data, and provide our conclusions.

2. Experimental setup

The experimental setup is displayed in figure 1. The experimental cell is 200 mm wide, 200 mm tall and 3.5 mm in depth. It is composed of two parts, the top and the bottom, separated by a thick band-like porous sponge (2 mm thick, 45 mm wide and 20 mm tall Tesa sponge 55604-00007), which is placed horizontally, i.e., gravity is perpendicular to the sponge. On top of it, approximately 25000 monodisperse brass spheres, of diameter $d = 350\,\mu$m, are deposited. The

sponge is hard enough to sustain the entire granular layer without bending or moving. Its typical pore size is of the order of 100 μm, thus grains cannot go through it. The height of horizontal layer made by the deposited grains is about 1.7 mm. Thus, the granular bed is about 570d wide, 6d in depth and 5d tall. Here, the sponge floor serves as a porous material for an air flow which, as it traverses the porous material, goes through an homogenization process before exciting with the granular layer.

The excitation of the layer is performed by means of a periodic air flow, which is generated by an air compressor (Mdent model Vicdent 1.1 HP) and is regulated by an electromechanical proportional valve (Teknocraft 203319) via a precision control regulator (Controlair 100) and an air lung. The response time of the valve is less than 4 ms. Its aperture is set by a variable voltage signal controlled by the first output of a two-channel function generator (RIGOL DG1022) through a power amplifier (NF model HFA4011). The proportional valve remains closed for an applied voltage lower than 4 V, and its maximum aperture is obtained at 27 V. The response of the valve possesses a very small hysteresis (less than 10% when an alternating voltage is delivered). The pressure oscillations induced by the variable air flow are measured before the flow enters the cell with a dynamic pressure sensor (PCB 106B) and a signal conditioner (PCB 480C02). Data is acquired using an acquisition card (NI-USB 6008) via Labview and is stored in a desktop computer for post-treatment. The proportional valve is connected to the dynamic pressure sensor through ten plastic hoses, sufficiently close to the experimental cell ($\sim$50 cm) such that the pressure drop between the measurement point and the actual cell air inlets is negligible ($<$1%). These inlets are located at the bottom of the cell, each separated from the others by 2 cm. The distance from the inlets to the lower part of the sponge is 30 cm, which is large enough to equalize spatially the local pressure fluctuations.

The alternating voltage applied to the proportional valve is a symmetrical triangular signal with a positive offset oscillating at a control frequency f_o, to generate a time-modulated reproducible pressure signal (as is shown in figure 2). The outgoing periodic air flow is far from a sinusoidal shape, as the one used in [18]: it serves the purpose of studying the response of a shallow granular bed to a non-harmonic periodic forcing. It can be noticed from the temporal trace of the pressure fluctuations that the granular layer is always excited by the periodic flow, and only during the large excursions occurring over a very short period of time where the layer is lifted from the sponge. In this sense, this situation is not different to the case of vibrofluidized granular systems, where the layer is effectively excited for very short periods of time in the cycle. Thus, we can think of our periodic excitation as a tapping type of forcing. As a control parameter of the experimental system, we compute the peak pressure amplitude P_o, which is the Fourier component of the pressure temporal trace related to the forcing frequency f_o, which is the most dominant component of the pressure oscillations. The measured P_o, as a function of the applied peak–peak voltage V_{pp} of the triangular signal, is shown in figure 2(b), and is roughly linear in all of the pressure range for any given frequency. A low level of hysteresis is observed within the range reported by the fabricator of the proportional valve. Thus, for our experimental setup, the control parameters are the forcing frequency f_o and the peak amplitude P_o of the pressure fluctuations at f_o. The extra pressure drop due to the motion and fluidization of the granular layer is negligible with respect to the one measured on the unloaded cell, thus making systematic calibration of the pressure fluctuations unnecessary.

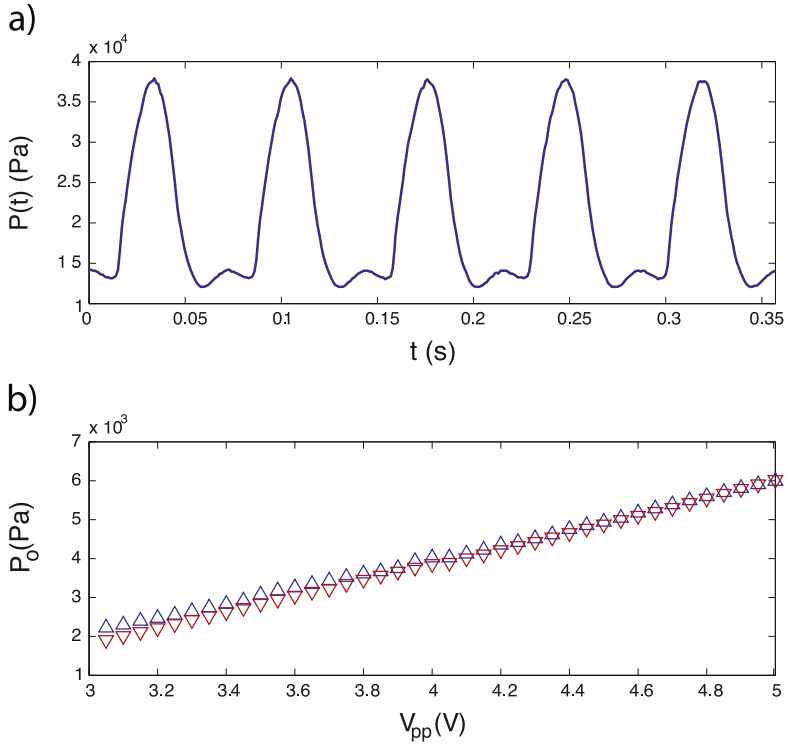

Figure 2. (a) A typical temporal trace of air flow pressure oscillations, which shows the tapping-like forcing. On the lower point of the pressure fluctuations, the layer resting on the sponge starts to dilate, and at the lowest maximum lifts itself from the sponge, to attain its maximum height half a foxing period later. In this state, the layer is completely dilated, showing the appearance of large density fluctuations (not shown here). In this case, the peak-to-peak voltage is $V_{\rm pp} = 5$ V and $f_o = 14$ Hz. (b) The peak pressure amplitude P_o versus $V_{\rm pp}$ obtained for increasing $(\triangle)$ and decreasing $(\triangledown)$ voltage ramps. For an increasing ramp, the calibration constant is 2082 Pa $\rm V^{-1}$, and for a decreasing ramp it is 1971 Pa $\rm V^{-1}$. In this case $f_o = 14$ Hz, the power amplifier gain is 20 and the voltage offset is 350 mV.

Images of the granular bed motion are acquired with a CCD camera (Pixelink PL-B741) over a 100 s time window in a 1200 × 200 px spatial window (with a 0.19 mm $\rm px^{-1}$ sensitivity in the horizontal direction and a 0.18 mm $\rm px^{-1}$ sensitivity in the vertical direction). White light from two high-power halogen lamps is sent through a diffusing screen from behind the granular layer as images are taken from the front. For each experimental configuration, two image sequences are taken. The first one, acquired at a high frame rate (100 fps), is used to study the typical oscillation frequencies of the granular layer, i.e., its fast dynamics. The second one, set at the subharmonic frequency $f_o/2$ using the second output of the function generator as a trigger, is used as a TTL signal to ensure a stroboscopic view of the oscillating layer in order to study its slow dynamics. For each acquired video, its sequence of images and the corresponding pressure signal are processed and analyzed with a desktop computer using MATLAB. The granular interface $y(x, t)$ is calculated for every point in space x at each time step t by an image

processing method where the granular layer surface profile is obtained for each image using a simple threshold intensity algorithm on a previously smoothed image, as is described in [18].

3. Experimental results

In this section, we describe the experimental observations of the shallow granular layer that was parametrically excited by a periodic air flow, performed on our experimental setup as we change f_o and P_o.

3.1. Granular parametric instability

We conducted experiments in the parameter space of P_o ranging from 100 Pa to 10 kPa and f_o ranging from 5 to 20 Hz. We concentrated our studies in the frequency range $f_o \in \left[12,\ 15\right]$ Hz, as the phenomenology is quite reproducible and less input pressure is needed. We will first focus on the homogeneous layer dynamics. In [18], a reduced cell was used to study solely the homogeneous state, as difficulties were found in creating it without any other structures interacting with it. This difficulty was overcome by increasing the offset voltage of the proportional valve by 75%, which created fewer kinks, making it possible to observe the homogeneous state without any kinks unless they were desired . Thus, larger peak pressures are needed to excite the granular layer. For a fixed value of f_o, increasing P_o induces small local displacements of the grains in the layer (of less than a diameter), which are seen as density fluctuations in the bulk of the granular layer. At the surface of the layer, larger fluctuations are observed as fewer collisions between grains occur. This motion is enhanced as P_o increases, lifting the complete layer over each period of the pressure oscillations, and increasing the local density fluctuations of the granular layer. For a critical value of $P_o = P_o^c$ dependent on f_o, the flat oscillating layer becomes unstable to small perturbations through a parametric instability, displaying subharmonic oscillations at $f_o/2$ [19].

With this critical value, the bifurcation parameter $\varepsilon = \left(P_o - P_o^c\right)/P_o^c$ is defined for the analysis above. In this setup, the granular layer presents an effective parametric resonance as a consequence of the forcing: the periodic air flow is responsible for inducing the oscillatory behavior of the layer and its respective parametric resonance [20]. This subharmonic response can be understood by measuring the spatially averaged motion of the granular interface $y\left(x,\ t\right)$ as a function of time t:

$$\bar{y}\left(t\right) = \frac{1}{L}\int_0^L y\left(x,\ t\right)dx,$$

where L is the width of the acquired image of the experimental cell. For $\varepsilon < 0$ the power spectral density (PSD) of $\bar{y}\left(t\right)$ displays a peak on f_o showing the harmonic character of the oscillation (cf figure 3, lower inset). As ε goes from negative to positive values, a subharmonic oscillation appears. For each excitation frequency there is a transition from harmonic to subharmonic dominant oscillations of the flat layer as P_o surpasses a critical value P_o^c ($\varepsilon > 0$), which is displayed by the continuous line in figure 3. This transition is found to be smooth and supercritical in nature for all frequencies in the observed experimental range. The value of P_o

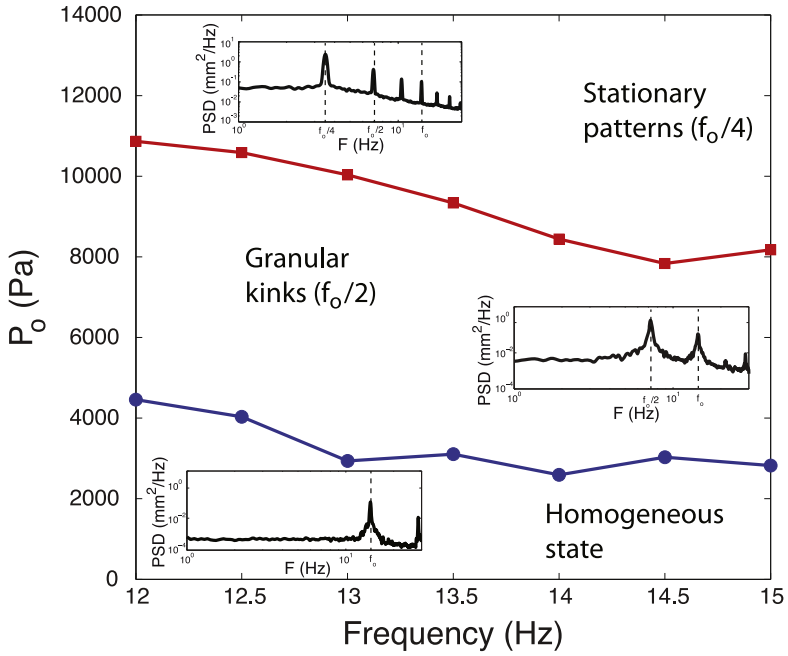

Figure 3. Parametric instability curves. The continuous line with circles (○) shows the experimentally computed phase line P_o^c as a function of f_o for the first parametric instability of the homogeneous layer. For $P_o < P_o^c$, only harmonic oscillations of the flat layer are present. For $P_o > P_o^c$, subharmonic oscillations are dominant, arising from a parametric instability. Above this line, the continuous line with squares (□) shows the experimentally computed phase line P_o^s as a function of f_o for the secondary parametric instability of the homogeneous layer. For $P_o^c < P_o < P_o^s$, subharmonic oscillations dominate the oscillating layer, showing kinks as a result. For $P_o > P_o^s$, a stationary pattern oscillating at $f_o/4$ is dominant, arising from a secondary parametric instability of the oscillating layer. For each type of behavior, a temporal power spectral sensity (PSD) of the dominant oscillations of the layer excited at $f_o = 14$ Hz is shown.

where the flat interface displays the parametric instability roughly decreases with f_o. Here, in what follows, f_o will be fixed at 14 Hz.

To describe this smooth transition from harmonic to subharmonic oscillations, we have chosen as the order parameter the amplitude of the subharmonic response of the layer. The temporal evolution of the amplitude is computed as follows. From each image, the spatial average of the surface profile curve $\bar{y}(t)$ is computed following the above prescription. The spectral content of this temporal trace is studied via its power spectrum density (PSD), which shows a mean peak at f_o (the forcing frequency) and the appearance of a secondary one at $f_o/2$, as the transition is surpassed (cf figure 3). Filtering the temporal signal around $f_o/2$ within a 1 Hz bandwidth, the global subharmonic oscillation of the layer is studied. The amplitude of this oscillation A, due to the intrinsic noisy character of this fluidized granular system, is a temporally fluctuating quantity that will be studied statistically.

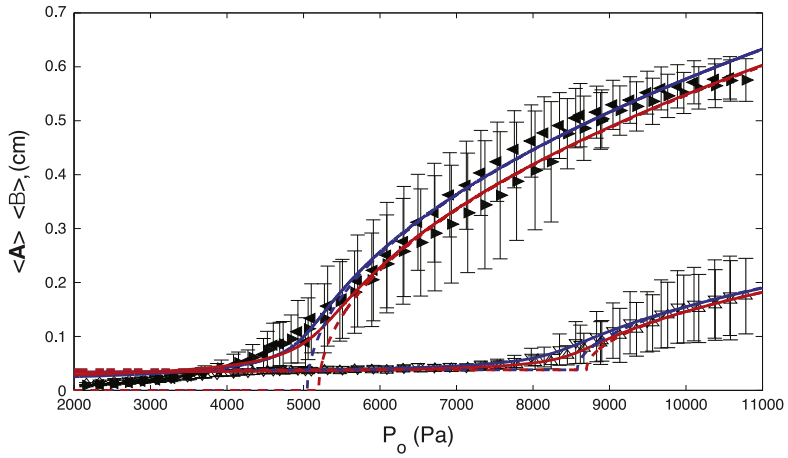

Figure 4. Main: Bifurcation diagrams for A and B as a function of P_o for $f_o = 14$ Hz. Here A is the amplitude of the subharmonic oscillations of the granular layer, and B is the amplitude of the stationary patterns oscillating at $f_o/4$. The full symbols correspond to $\langle A\rangle$ for increasing $(\triangleright)$ and decreasing $(\triangleleft)$ values of P_o. The open symbols correspond to $\langle B\rangle$ for increasing $(\triangle)$ and decreasing $(\triangledown)$ values of P_o. Error bars for both data sets correspond to $\sigma(A)$ and $\sigma(B)$, respectively. For the A data set, the dashed line corresponds to the theoretical supercritical fit $\langle A\rangle = \alpha_A\left(P_o - P_o^c\right)^{1/2}$, with $\alpha_A = 7.9 \pm 0.2$ cm kPa$^{1/2}$ and $P_o^c = 5050 \pm 160$ Pa for increasing P_o, and $\alpha_A = 8.1 \pm 0.3$ cm kPa$^{1/2}$ (dark line) and $P_o^c = 5140 \pm 170$ Pa for decreasing P_o (gray line). The continuous line corresponds to the theoretical fit [21] $\langle A\rangle = \alpha_A\left(\left(\left(P_o - P_o^c\right) + \left(\left(P_o - P_o^c\right)^2 + 2\eta_A\right)^{1/2}\right)\Big/2\right)^{1/2}$, where $\eta_A = 14592 \pm 560$ Pa^2 for increasing P_o (dark line) and 18349 ± 700 Pa^2 for decreasing P_o (gray line) stands for the noise intensity of the fluctuating granular layer. For the B data set, the dashed line corresponds to the theoretical supercritical fit $\langle B\rangle = \alpha_B\left(P_o - P_o^s\right)^{1/2}$, with $\alpha_B = 3.1 \pm 0.2$ cm kPa$^{1/2}$ and $P_o^s = 8640 \pm 205$ Pa for increasing P_o, and $\alpha_B = 3.0 \pm 0.2$ cm kPa$^{1/2}$ (dark line) and $P_o^s = 8783 \pm 145$ Pa for decreasing P_o (gray line). The continuous line corresponds to the theoretical fit similar to the one in [21] $\langle B\rangle = \alpha_B\left(\left(\left(P_o - P_o^c\right) + \left(\left(P_o - P_o^c\right)^2 + 2\eta_B\right)^{1/2}\right)\Big/2\right)^{1/2} + B_o$ where $\eta_B = 20459 \pm 600$ Pa^2 and $B_o = 0.038 \pm 0.005$ cm FOR increasing P_o (dark line), and 19050 ± 804 Pa^2 and $B_o = 0.033 \pm 0.007$ cm for decreasing P_o (gray line). Here B_o stands for acorrective root-mean-squared base level coming from the computation of B from the spatial PSD of $y(x, t)$.

From the temporal trace of the filtered subharmonic oscillation $A\cos\left(\pi f_o t\right)$, we compute its temporal average (mean value) $\langle A\rangle$ and its standard deviation $\sigma_A \equiv \sqrt{\langle A^2\rangle - \langle A\rangle^2}$, respectively. Figure 4 shows the typical bifurcation diagram for $\langle A\rangle$ as a function of P_o. The symbols stand for $\langle A\rangle$ and error bars for $\sigma(A)$. The amplitude of the subharmonic pattern grows

Table 1. Fitting parameters for the average values of $\langle A \rangle$ and $\langle B \rangle$ following the fitting scheme proposed in [21].

$\langle X \rangle$ (cm)	α, β (cm kPa$^{-1/2}$)	$P_o^{(c)}$, $P_o^{(s)}$ (kPa)	η $\left(10^{-3} \times \text{kPa}^2\right)$	A_o, B_o (mm)
$\langle A \rangle$ for $P_o \nearrow$	7.9 ± 0.2	5.05 ± 0.16	14.59 ± 0.56	—
$\langle A \rangle$ for $P_o \searrow$	8.1 ± 0.3	5.14 ± 0.17	18.35 ± 0.70	—
$\langle B \rangle$ for $P_o \nearrow$	3.1 ± 0.2	8.64 ± 0.21	20.46 ± 0.60	0.38 ± 0.05
$\langle B \rangle$ for $P_o \searrow$	3.0 ± 0.2	8.78 ± 0.15	19.05 ± 0.80	0.33 ± 0.07

smoothly from almost zero, which is related to the minimal discretization of the pattern. No abrupt change is evident, so no critical value of P_o is found for this transition. No discernible hysteresis loop is observed between the increasing and decreasing P_o ramps. Thus, the inherent noise present in the fluidized granular bed changes the qualitative form of the supercritical bifurcation diagram [21].

The experimental data can be fitted following a simple model that takes into account the noisy character of the supercritical bifurcation of $\langle A \rangle$ [21]. The model predicts the most probable value as a function of the bifurcation point of the deterministic system, related to P_o^c, and the noise intensity, related to the inherent granular fluctuations of the layer [17, 18, 22]. These parameters do not change drastically between increasing and decreasing P_o ramps (increasing values for P_o lie within the confidence interval of the increasing value of P_o, and vice versa). Figure 4 shows the theoretical fits with (continuous line) and without (dashed line) noise. The dashed lines correspond to the deterministic bifurcation diagram obtained from a theoretical prediction without noise: $\langle A \rangle = \alpha_A \left(P_o^c\right)^{1/2} \varepsilon^{1/2}$, where α_A is a calibration factor and $\varepsilon = \left[\left(P_o - P_o^c\right)/P_o^c\right]$ is the reduced control parameter calculated using the adjusted parameters with the theoretical prediction with noise. These curves fit our data quite well close to the bifurcation point P_o^c for increasing and decreasing P_o. The fitting parameters are summarized in table 1. For every f_o in our experiments, all bifurcation curves follow the above expression. The spatial structure of the granular layer was also studied to characterize the stationary states as the layer oscillates. For $P_o < P_o^c$ ($\varepsilon < 0$), the harmonically oscillating flat layer displays no typical spatial scale.

For $P_o > P_o^c$ ($\varepsilon > 0$), fluctuations of the flat layer display a characteristic wavelength and frequency sporadically (see figure 1), disappearing randomly with a typical lifetime of the order of the forcing period, which is known as a *precursor* [23]. The development of a precursor on the surface of the granular layer is a consequence of internal fluctuations coming from the energy input of the air flow, which excites the slowest decaying spatial mode of the uniform steady state of the layer interface. Thus, fluctuations can create locally a random amplitude perturbation with a given wavelength that will decay. The process is repeated constantly at the surface. This type of supercritical noisy bifurcation has also been observed in vibrofluidized granular layers, although the analysis of the transition was performed via the spectral properties of the fluctuations [24]. In our experimental setup, the typical wavelength λ of the precursor is typically $\sim$2 cm. No discernible change is observed for our experimental control parameters. We have checked that λ is independent of the periodicity or the position of the air inlets. It must be noted that although no discernible inhomogeneities have been observed on the granular layer

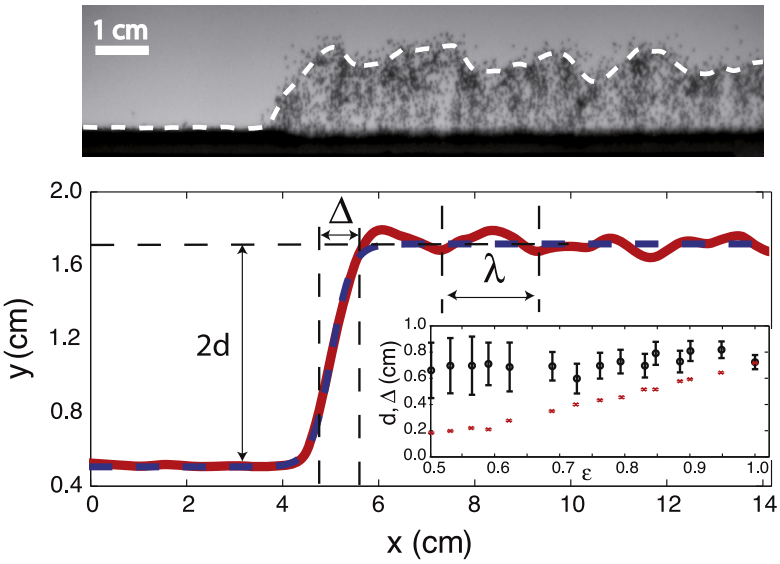

Figure 5. Top: typical image of a granular kink at $P_o = 8038 \pm 20$ Pa ($\varepsilon = 0.59 \pm 0.01$). The dashed line is the numerical interface detection. Middle: granular kink averaged over 1000 frames. Here, d stands for the granular kink height with respect to the middle plane, Δ stands for the typical core size of the kink and λ is the average wavelength of the homogeneous state. Inset: granular kink height d (×) and typical core size Δ (○) as a function of ε. The error bars stand for the standard deviation for d and Δ for each value of ε.

dynamics, the existence of such non-uniformities either on the air flow or in the sponge, and thus on the precursor structure, cannot be discarded through our measurements.

3.2. Granular kinks

Now, we will concern ourselves with kinks appearing through the above-described transition in the extended cell. Increasing $\varepsilon > 0$, the subharmonic motion described above allows the system to exhibit bistability between two homogeneous states that are out of phase. This means that the subharmonic motion permits the oscillation of the layer either in phase or out of phase with respect with the forcing. This bistability can be used to create a spatial connection between them. More precisely, there is a height jump as we go from one side of the cell to the other through a finite region of the layer where this shift occurs. This means that, at any given instant, on one side of the region the granular layer is moving upwards and on the other side it is moving downwards. The connection between both homogeneous phases is termed *kink*. A kink appears spontaneously at any point of the experimental cell. By choosing the phase mismatch between the triggering signal and the layer oscillation, the kink can be imaged when the separation between the in-phase and out-of-phase parts of the granular oscillating layer is at its maximum. This triggering signal comes from the second output of the two-channel frequency generator as a TTL voltage. For each ϵ, a set of 1000 images is used to average all the computed interfaces in an image sequence. The averaged front interface, its height d and its width Δ for different P_o are shown in figure 5. Here, 2d corresponds to the distance between the in-phase and out-of-phase states, measured at its maximum separation. Δ is computed as the average width of the spatial derivative of the kink solution. In our experimental runs, d grows linearly with ε, and

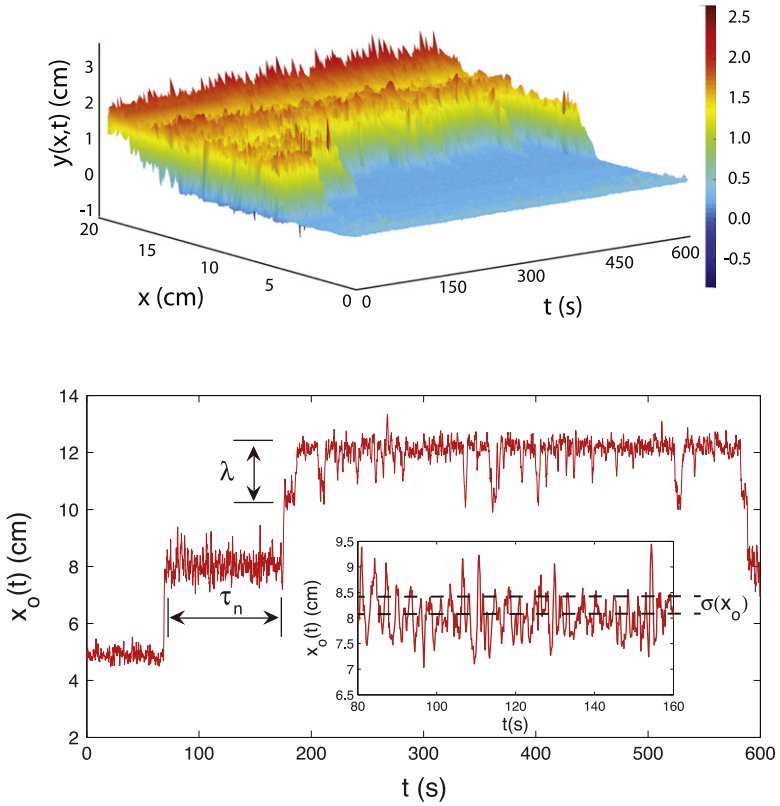

Figure 6. (a) An image sequence of 10 minutes of $P_o = 5720 \pm 20$ Pa ($\varepsilon = 0.13 \pm 0.01$). (b) The temporal trace of the core of the kink $x_o(t)$ as a function of time. λ is the typical fluctuating wavelength of the precursor of the homogeneous state and τ_n is nth time lag between jumps of $x_o(t)$. Inset: the temporal trace displaying the typical fluctuations of $x_o(t)$ around an equilibrium. The standard deviation of $x_o(t)$ is given by $\sigma(x_o)$.

Δ is independent of ε as already shown in [17]. These scaling laws have not been found in other experimental or theoretical studies. For instance, they are not the same ones calculated from the simple supercritical model for parametrically excited kinks presented in [5, 6, 16], which predict that $d \sim \varepsilon^{1/2}$ and $\Delta \sim \varepsilon^{-1/2}$. Note that both the in-phase and out-of-phase states present a spatial modulation on the homogeneous phases, which is the same one discussed above. The typical wavelength of the kink is again λ (cf figure 5). Increasing further the number of images used in the average values of d from 1000 to 10000, Δ and λ do not affect their computed values.

Fluctuations are always present in the dynamics of the granular layer affecting the morphology of the kink. Indeed, the inherent noise of the layer determines both the appearance of a precursor on the homogeneous states and the spatiotemporal fluctuations of the kink profile. These fluctuations dictate the long-term dynamics of the spatially modulated kink. A typical image sequence of the kink motion acquired over long time periods ($\sim 10^4$ periods of oscillation) is depicted in figure 6(a), where the complete structure shifts its position in the experimental cell through discrete jumps. This motion is tracked in time by following the kink

position, $x_o(t)$, which is the position in space where the spatial derivative of the kink reaches its maximum [25].

The typical distance between these jumps is λ (cf figure 6(b)), and they occur at random moments in time either to the left or the right of the cell. Although the kink displays these jumps, the temporal average of $x_o(t)$, $\langle x_o \rangle$, does not change in the experimental observation time. Hence, the dynamics of $x_o(t)$ can be understood as a random motion (where fluctuations come from the inherent noise of the granular layer and the tortuous structure of the air flow within the layer) within a periodical potential (arising from the spatial structure of the precursor) [26]. It can be foreseen that in the case of the existence of a small asymmetry in the system (for instance, tilting the cell) the dynamics can be described as a Brownian-type motor [27, 28]. We have characterized the statistics of these jumps as a function of P_o for a granular kink. To do so, we have measured the series of time lags $\{\tau_n\}_{n=1}^{N}$ between jumps of $x_o(t)$ from one equilibrium position to another in long experimental runs of 40 minutes (cf figure 6(b)). As $P_o > P_o^c$ increases, the number of jumps per run, N, decreases rapidly. Data is presented here for $N \geqslant 3$. For $P_o \simeq P_o^c$, it is very difficult to establish a stable kink for the whole experimental run: several kinks appear and disappear within the strongly fluctuating granular layer. Experimentally reproducible results are observed for $P_o \geqslant 5.5$ kPa. For $P_o > 7$ kPa, the typical time lag between jumps is larger than the experimental run time, thus no relevant data is shown here for P_o larger that 7 kPa. The mean residence time, i.e., the mean time lag between jumps, $\langle \tau \rangle$, is computed for each image sequence, as shown in figure 7(a). $\langle \tau \rangle$ grows roughly as an exponential of the applied peak pressure. It must be noticed that the root-mean-square fluctuations of such jumps $\sigma(\tau)$ are of the same order as $\langle \tau \rangle$ (not shown here), which means that as $\langle \tau \rangle$ increases, so do the typical fluctuations of each τ_n around $\langle \tau \rangle$.

Using the same front tracking algorithm, the local fluctuations of $x_o(t)$ are denoted $\sigma(x_o)$ (cf figure 6(b)). To compute $\sigma(x_o)$, the local fluctuations of $x_o(t)$ at each equilibrium state are added up. An equilibrium state for $x_o(t)$ is a position in space where the kink rests within a vicinity of a size smaller than $\lambda/2$. These fluctuations decrease slightly with increasing P_o, as can be shown in figure 7(b), remaining almost constant throughout the range of applied P_o. The complete statistics of $\{\tau_n\}_{n=1}^{N}$ and $x_o(t)$ require longer experimental runs ($\sim 10^5$–10^6 s), but their first cumulants can be correctly approximated by the acquired data.

3.3. Spatial structure of the granular layer and secondary instabilities

The spatial structure of the surface granular layer fluctuations can be studied by computing its spatial PSD for different values of ε above the parametric instability threshold, as is shown in figure 8. Here, PSDs are computed when the layer reaches its maximum height and they are normalized by the variance of the surface fluctuations of the complete image sequence $\sigma(y)^2$, defined as above. We also show the dependence of the typical wavelength λ on ε, computed from the PSDs. The resolution of the wavelength is highly quantized due to our optical and physical resolution ($\sim$0.3 cm). For peak pressure values $P_o < 8$ kPa ($\varepsilon < 0.8$), the precursor appears over the homogeneous layer displaying a wavelength λ observed in the PSD $\lambda \sim 2$ cm,

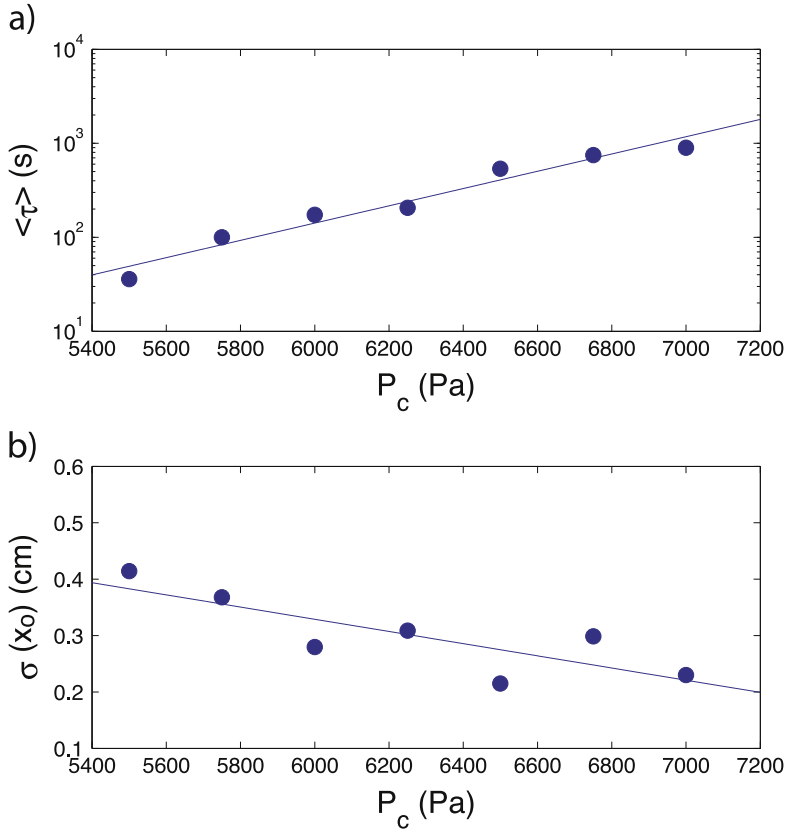

Figure 7. (a) Semilogarithmic plot of the mean residence time $\langle\tau\rangle$ versus P_o (○). The continuous line shows the exponential best fit with a slope 2.1×10^{-3} Pa^{-1}. Error bars are not shown as they are of the same order as $\langle\tau\rangle$ (not shown here). (b) Standard deviation of the core of the kink position $\sigma\left(x_o\right)$ versus P_o (○). The continuous line shows the best fit with a slope -10^{-4} cm Pa^{-1}. Error bars for η are of the order of 0.05 cm Pa^{-1} (not shown here).

which increases slightly with ε. From the non-dimensionalized data, a rough estimate of the amplitude of the precursor can be given by integrating below the shallow peak of the precursor between 0.3 and 0.6 cm^{-1}. The area under the curve grows roughly linearly with P_o (not shown here), and thus the amplitude of the non-dimensionalized precursor grows roughly with $\varepsilon^{1/2}$. It must be noted that the growth of the precursor amplitude has been computed without the normalization by $\sigma\left(y\right)^2$, finding the same scaling with ε.

For $P_o \geqslant 8$ kPa ($\varepsilon \geqslant 0.6$), the homogeneous layer that was oscillating at $f_o/2$ (and thus the granular kink) develops a smooth supercritical secondary instability where a highly nonlinear pattern state appears over the entire experimental cell with a wavelength $\sim$3 cm. This wavelength, which increases slightly with ε, is computed from the PSDs shown in figure 9, and it is larger than the typical wavelength of the granular precursor. The PSDs in figure 9 are computed for two distinct stages in time of the layer oscillation cycle. Figure 9(a) shows the spatial fluctuations of the dilated layer, i.e., when the layer reaches its maximum height and, thus, the dilation of the layer is at its maximum. Figure 9(b) shows the spatial fluctuations of the

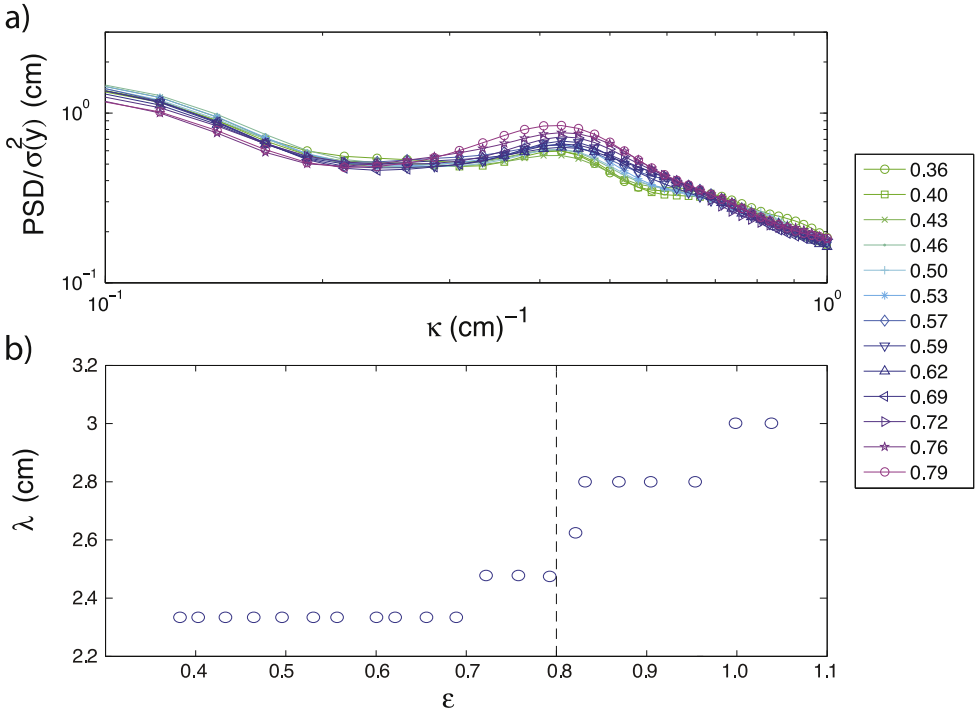

Figure 8. (a) Normalized power spectral density of the spatial fluctuations of oscillating layer PSD/$\sigma(y)^2$ as a function of the inverse wavelength $1/\lambda$ for increasing ε from 0.36 to 0.79 for the dilated homogeneous layer. b) λ as a function of ε for increasing ε from 0.36 to 1.09 for the dilated homogeneous layer. The vertical dashed line corresponds to the zone where the precursor is found.

compacted layer when the layer is at repose. The structure of the pattern is similar to the one displayed in [11], where localized streams of grains are ejected upwards periodically. These streams are focalized regions of the order of 1 cm, where grains are expelled upwards following a shape very similar to a granular jet [11] reaching a typical height of 3 cm. The streams change position along the cell periodically with a wavelength ∼3 cm. The oscillating frequency of this pattern is 3.5 Hz ($f_o/4$), i.e., it appears as subharmonic instability of the parametrically amplified layer oscillating a $f_o/2$. This oscillation frequency is observed from the stroboscopically acquired image sequence at $f_o/2$: two consecutive frames show that the maxima of the pattern structure is displaced half a wavelength. The transition from the homogeneous layer oscillating at the subharmonic frequency $f_o/2$ to the pattern oscillating at $f_o/4$ is smooth and supercritical, in the same fashion as the one described above (cf figure 4). Furthermore, it can be seen that this transition is coupled directly to the underlying subharmonic oscillation, as $\sigma(A)$ decreases strongly when the stationary pattern develops. A similar transition has been observed in two-dimensional vibrated shallow granular layers [29]. Using the same fitting scheme, we find the critical value of the peak pressure for this instability, P_o^s. The dashed lines correspond to the deterministic bifurcation diagram obtained from a theoretical prediction without noise, $\langle B\rangle = \alpha_B\left(P_o^s\right)^{1/2}\varepsilon^{1/2} + B_o$, where α_B is a calibration factor, $\varepsilon = \left[\left(P_o - P_o^s\right)/P_o^s\right]$ is the reduced control parameter calculated using the adjusted parameters with the theoretical

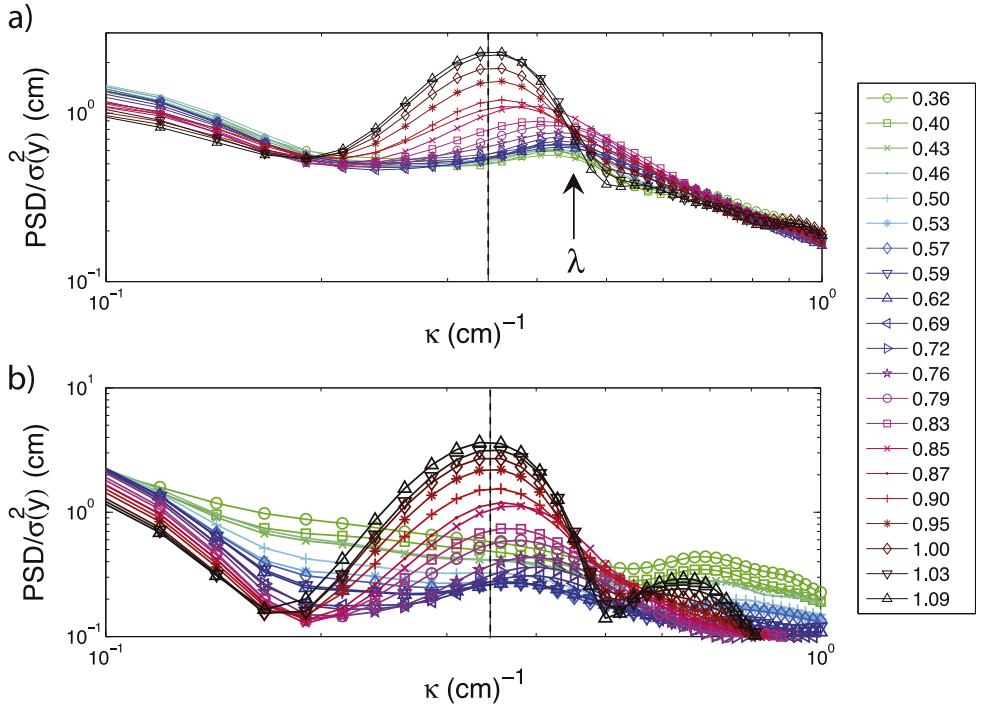

Figure 9. (a) Normalized power spectral density of the spatial fluctuations of the oscillating layer PSD/$\sigma\left(y\right)^2$ as a function of the inverse wavelength $1/\lambda$ for increasing ε from 0.36 to 1.09 for the dilated homogeneous layer. (b) The normalized power spectral density of the spatial fluctuations of the oscillating layer PSD/$\sigma\left(y\right)^2$ as a function of the inverse wavelength $1/\lambda$ for increasing ε from 0.36 to 1.09 for the compacted homogeneous layer. The vertical dashed lines correspond to the wavelength of the stationary wave pattern.

prediction with noise, and B_o is a base line level. These curves fit our data quite well close to the bifurcation point P_o^s for increasing and decreasing P_o. The pattern appears at $P_o^s = 8640 \pm 205$ Pa for increasing P_o, and at $P_o^s = 8783 \pm 145$ Pa for decreasing P_o. For other frequencies this transition was observed, although qualitative measurements are lacking. It is important to note that the base level of the pattern amplitude is nonzero, mainly due to the presence of larger surface fluctuations as larger values of P_o are used.

4. Discussions and conclusions

In this section, we will discuss a theoretical description of the granular kink dynamics through the use of a Brownian particle-type model moving in a periodic potential, and then we will draw conclusion from these considerations.

4.1. Brownian dynamics

The dynamics of defects, interfaces and fronts have been widely studied in the literature (see [6] and references therein). In order to understand the dynamics of the granular kink and its evolution, we present a very simple particle-type model based on the above data. Particle-type

models describe correctly the long-time evolution of extended systems in the presence of defects and interfaces [4, 6]. Physical systems such as magnetic materials [8] display defects, termed wall domains, where their reduced dynamics can be thought of as a particle-type one, even in the presence of thermal fluctuations. In our system, we observe that the granular kink possesses a modulation arising from the spatial structure of the inherent fluctuations displayed by the homogeneous states—*the precursor*—affecting its ulterior evolution. The effective amplitude of the precursor (cf figure 9) scales with $\varepsilon^{1/2}$, as stated above. We also observed that the dynamics of the core of the kink can be described by the position of its core, $x_o(t)$, which fluctuates around equilibria, residing close to them for times longer than 10–100 oscillation periods. After this time has elapsed, $x_o(t)$ jumps to other equilibria through large excursions either to the left or to the right with equal chance. From our data, we estimate the typical scale of fluctuations around equilibria $\sigma(x_o) \sim 0.3\,\text{cm} \ll \lambda$. With this in mind, we propose a description of the dynamics of $x_o(t)$ as a Brownian particle in a potential well [26, 30]

$$\dot{x}_o(t) = -\frac{\partial U(x_o)}{\partial x_o} + \sqrt{\eta}\,\zeta(t), \tag{1}$$

where $U(x_o)$ is an effective symmetrical potential coming from the precursor of the homogeneous states. The spatial periodicity of $U(x_o)$ is given by λ (the dominant wavelength of the precursor), and its scale is proportional to ε (the typical amplitude of the precursor). Thus, for simplicity, we will model the potential as $U(x_o) = U_o \cos(\kappa x_o + \phi)$, with $U_o > 0$ the potential barrier scale proportional to ε, $\kappa = 2\pi/\lambda$ the typical wave vector of the potential and ϕ a phase which can be set to zero by shifting the origin of the spatial coordinate. η is the noise intensity of the local fluctuations and $\zeta(t)$ is a Gaussian process with zero mean, $\langle \zeta(t) \rangle = 0$, and the delta autocorrelation function in time $\langle \zeta(t)\zeta(t') \rangle = \delta(t - t')$. Close to any equilibria (a minimum of the potential), the local dynamics can be reduced to

$$\dot{x}_o(t) = -\kappa^2 U_o x_o + \sqrt{\eta}\,\zeta(t), \tag{2}$$

which is the relaxation evolution of a Brownian particle [30]. Integrating directly equation (2), which is linear in x_o, we find that the root-mean-square fluctuations of x_o, $\sigma(x_o) = \sqrt{\frac{\eta}{2\kappa^2 U_o}}$.

On the other hand, due to the presence of fluctuations in the system, $x_o(t)$ can explore other equilibria. This is done by using these fluctuations to overcome the potential barrier that separates these equilibria, which in this case is U_o. The time it takes $x_o(t)$ to escape one of this wells for the first time, τ, is a random variable, as it can be longer or shorter depending on the realization of the noise. The average of τ, $\langle \tau \rangle$, is termed the mean first passage time of the system [26, 30, 31], and it can calculated in the limit of weak noise intensity η from the Dynkin equation [26, 30, 32, 33]. Its form is an exponential, much to the resemblance of the Arrhenius rate in chemical kinetics [30]. In this limit

$$\langle \tau \rangle = \sqrt{\frac{\pi^2}{|U''(x_b)|U''(x_a)}} \times e^{(U(x_b)-U(x_a))/\eta}, \tag{3}$$

where x_b and x_a are consecutive maxima and minima of $U\left(x_o\right)$ separated by $\lambda/2$, and $U''\left(x_o\right)$ is the second derivative of the potential evaluated at x_o. The absolute value in the prefactor comes from the fact that the second derivative of the potential at its maximum is negative. Thus, using our simple model, the mean first passage time reads

$$\langle\tau\rangle = \sqrt{\frac{\pi^2}{\kappa^4 U_o^2}} \times e^{Uo/\eta}. \tag{4}$$

In this case, $\log\left(\langle\tau\rangle\sqrt{\frac{\kappa^4 U_o^2}{\pi^2}}\right) = \frac{U_o}{\eta}$. From $\sigma\left(x_o\right)$ and $\langle\tau\rangle$ we can deduce the type of potential and noise intensity we need in order to model the dynamics of $x_o\left(t\right)$. Our experimental data gives $\log\left(\langle\tau\rangle\right) \propto P_o$, and $\sigma\left(x_o\right)$ is slightly decreasing with P_o in the experimental range. Arranging the terms as a function of $\varepsilon = \left(P_o - P_o^c\right)/P_o^c \ll 1$, we find $U_o/\eta \sim 10\left(1+\varepsilon\right)$, and $\sigma\left(x_o\right) \sim \lambda\left(1-\varepsilon/2\right)\big/\sqrt{80\pi^2} \simeq 0.1$ cm and decreasing slightly with ϵ within the experimental range. Hence, equation (1) describes correctly the observed fluctuating dynamics of the core of the spatially modulated kink as a Brownian motion in a periodic potential. In this sense, the inherent granular fluctuations generate an effective periodic potential $U\left(x_o\right)$ coming from the precursor and, also, the necessary noise needed for the exploration of other equilibria of the potential, represented by its intensity η. As the precursor increases its amplitude, so does the amplitude of the effective potential U_o, and thus $\langle\tau\rangle$ grows exponentially and $\sigma\left(x_o\right)$ decreases slightly. We can relate $U\left(x_o\right)$ and η directly with the existence and properties of the precursor, but if specific dependence of U_o and η on ε is desired, another relation is needed, as the expressions found above are dependent on the ratio U_o/η.

4.2. Conclusions

The fluidized shallow granular layer presents several structures depending on the applied peak pressure P_o and frequency f_o of the periodic air flow. We have focused our study on spatially modulated granular kinks appearing via a parametric instability of the homogeneous state oscillating at the forcing frequency, their structure and dynamics. The typical height of the kink grows linearly with P_o, and its width remains roughly constant in the experimental range of P_o. The kink does not remain stationary and shifts its position, characterized by its core $x_o\left(t\right)$. The long-time evolution of $x_o\left(t\right)$ can be described as a Brownian particle in the presence of a random noise of intensity η in an effective periodic potential $U\left(x_o\right)$. The inherent fluctuations of the Brownian motion, and the amplitude and periodicity of the effective potential, are given by the fluctuating spatiotemporal properties of the granular layer. As a final remark, we have left out the dynamics and evolution of other structures displayed by the layer, such as stationary patterns oscillating at $f_o/4$ and their interaction with other relevant modes, as they lie outside the scope and focus of this manuscript. Work in describing the interaction of such structures with kinks, and their evolution, is in progress.

Acknowledgments

The authors would like to thank M G Clerc and N Verschueren for fruitful discussions. This work was supported financially by ACT-127, ANR-CONICYT 39 and FONDECYT grant 113 0354.

References

[1] de Gennes P G 1999 *Rev. Mod. Phys.* **71** 374
[2] Aranson I S and Tsimring L S 2006 *Rev. Mod. Phys* **78** 641
[3] Jaeger H M, Nagel S R and Behringer R P 1996 *Rev. Mod. Phys.* **68** 1259
[4] Nicolis G and Prigogine I 1977 *Self-Organization in Non Equilibrium Systems* (New York: Wiley)
[5] Pismen L M 2006 *Patterns and Interfaces in Dissipative Dynamics (Springer Series in Synergetics)* (Berlin: Springer)
[6] Cross M C and Hohenberg P C 1993 *Rev. Mod. Phys.* **65** 851
[7] Pomeau Y 1986 *Physica* **23D** 3
[8] Manton N and Sutcliffe P 2004 *Topological Solitons* (Cambridge: Cambridge University Press)
[9] Landau L D and Lifshiftz E M 1976 *Mechanics* (Oxford: Pergamon)
[10] Fauve S 1984 *Hydrodynamics and Nonlinear Instabilities* ed C Godrèche and P Manville (New York: Springer)
[11] Aronson I and Tsimring L 2009 *Granular Patterns* (New York: Oxford University Press)
[12] Douady S, Fauve S and Laroche C 1989 *Europhys. Lett.* **8** 621
[13] Moon S J, Shattuck M D, Bizon C, Goldman D I, Swift J B and Swinney H L 2001 *Phys. Rev.* E **65** 011301
Moon S J, Goldman D I, Swift J B and Swinney H L 2003 *Phys. Rev. Lett.* **91** 134301
[14] Peng Z, Guo-Qing M, Kai H, Yi Y and Rong-Jue W 2005 *Chin. Phys. Lett.* **22** 1961
[15] Hui C, Wei-Zhong C and Guo-Qing M 2013 *Chin. Phys. Lett.* **30** 044501
[16] Coullet P 2002 *Int. J. Bif. Chaos* **12** 245
[17] Macías J E, Clerc M G, Falcón C and Garci-Ñustes M A 2013 *Phys. Rev.* E **88** 020210 (R)
[18] Ortega I, Falcón C, Clerc M G and Mujica N 2010 *Phys. Rev.* E **81** 046208
[19] Arnol'd V I 1989 *Mathematical Methods of Classical Mechanics* (New York: Springer)
[20] Clerc M G, Falcón C, Fernandez-Oto C and Tirapegui E 2012 *EPL* **98** 30006
[21] Agez G, Clerc M G and Louvergneaux E 2008 *Phys. Rev* E **77** 026218
[22] Garay J, Ortega I, Clerc M G and Falcón C 2012 *Phys. Rev.* E **85** 035201 R
[23] Schöpf W and Zimmermann W 1993 *Phys. Rev.* E **47** 1739
[24] Goldman D I, Swift J B and Swinney H L 2004 *Phys. Rev. Lett.* **92** 174302
[25] Kawasaki K and Ohta T 1982 *Physica* **116A** 573
Kawasaki K 1983 *Physica* **119A** 17
Kawasaki K 1984 *Ann. Phys.* **154** 139
[26] Risken H 1984 *The Fokker–Planck Equation* (Berlin: Springer)
[27] Reiman P and Hänggi P 2002 *Appl. Phys.* A **75** 169
[28] Clerc M G, Falcón C and Tirapegui E 2005 *Phys. Rev. Lett.* **94** 148302
Clerc M G, Falcón C and Tirapegui E 2006 *Phys. Rev.* E **74** 011303
[29] Melo F, Umbanhowar P B and Swinney H L 1995 *Phys. Rev. Lett.* **75** 3838
[30] van Kampen NG 2007 *Stochastic Processes in Physics and Chemistry* (Amsterdam: North Holland)
[31] Hängii P, Talkner P and Borkovec M 1990 *Rev. Mod. Phys.* **62** 251
[32] Gardiner C 2009 *Stochastic Methods: A Handbook for the Natural and Social Sciences* (New York: Springer)
[33] Dynkin E B and Juschkewitz A A 1969 *Sätze und Aufgaben über Markoffsche Prozesse* (Berlin: Springer)